

CHEMICAL PHYSICS

Anomalous interfacial dynamics of single proton charges in binary aqueous solutions

Jean Comtet^{1,2*}, Archith Rayabharam³, Evgenii Glushkov¹, Miao Zhang¹, Ahmet Avsar⁴, Kenji Watanabe⁵, Takashi Taniguchi⁵, Narayana R. Aluru^{3†}, Aleksandra Radenovic¹

Our understanding of the dynamics of charge transfer between solid surfaces and liquid electrolytes has been hampered by the difficulties in obtaining interface, charge, and solvent-specific information at both high spatial and temporal resolution. Here, we measure at the single charge scale the dynamics of protons at the interface between an hBN crystal and binary mixtures of water and organic amphiphilic solvents (alcohols and acetone), evidencing a marked influence of solvation on interfacial dynamics. Applying single-molecule localization microscopy to emissive crystal defects, we observe correlated activation between adjacent ionizable surface defects, mediated by the transport of single excess protons along the solid/liquid interface. Solvent content has a nontrivial effect on interfacial dynamics, leading at intermediate water fraction to an increased surface diffusivity, as well as an increased affinity of the proton charges to the solid surface. Our measurements evidence the notable role of solvation on interfacial proton charge transport.

INTRODUCTION

Understanding the dynamics and transport of charges at solid/liquid interfaces is key to a number of physical, biological, and chemical processes, ranging from biophysical transport (1, 2) and nanofiltration (3, 4) to energy harvesting (5, 6), energy storage (7), catalysis (8, 9), and electrochemistry (10, 11). Interfacial charge dynamics is ultimately determined by physicochemical processes, such as dissociation of charged functional groups or specific adsorption of ions (12–15), which occur in the few layers of molecules at the interface between the solid surface and the solvent. While new insights have been obtained thanks to electrokinetic measurements (16, 17), second harmonic generation (18–20), dynamic atomic force microscopy (21), or time-resolved fluorescence (22, 23), our fundamental understanding of the dynamics of these interfacial processes remains poor (24, 25) because of the difficulties in obtaining surface-specific information at both high spatial and temporal resolution. In this context, we could recently resolve the diffusive dynamics of individual excess proton charge at the interface between defected hexagonal boron nitride (hBN) and aqueous solutions (26). By allowing the direct observation of proton charge transport the single-molecule scale under various solvent conditions, the application of single-molecule localization microscopy (SMLM) to the reactive optically active defects hosted at the hBN crystal surface has the potential to bring new general insights on the dynamics and transport of charges at solid/liquid interfaces.

The physicochemical and charge solvation properties of the solvent are expected to have a strong yet poorly understood effect on interfacial charge dynamics. In aqueous media, one facile route

to alter charge solvation and the hydrogen bonding structure is by mixing water with an organic amphiphilic solvent (e.g., acetone or alcohol such as methanol or ethanol) having both hydrophilic (polar —OH or =O) and hydrophobic (apolar alkyl —CH₃) moieties. These binary solutions show anomalous thermodynamic behavior in the bulk due to incomplete mixing at the molecular scale (27–30). The presence of hydrophobic alkyl groups hinders the participation of these organic molecules to the water hydrogen bonding networks (27) and modifies its topology, an effect that has been probed extensively through molecular dynamics simulations (28, 31–34). Because protons are transported in water along the H bonding network, their transport is also strongly affected by the presence of the organic solvent (35–38). The amphiphilic nature of protons, caused by the asymmetric charge distribution between the apolar oxygen lone pair and the hydrophilic H bonding sites, further leads to peculiar interaction with binary mixtures due to the asymmetric structure of the solvation shell (36, 38). Last, the behavior of these mixtures is further complexified at interfaces, with reports of self-assembly (39) and specific adsorption (40) at hydrophobic surfaces.

Here, we investigate, at the single charge scale, the complex relationship between solvation and proton charge dynamics at solid/liquid interfaces. We use spectral SMLM to probe the interface between a defected hBN crystal and binary mixtures of water and organic solvents (methanol, ethanol, and acetone). By varying the relative amount of water in the mixtures, we fine-tune hydrogen bonding in the liquid and probe how it affects proton charge dynamics at the hBN surface. We first show that spectral SMLM can serve as a chemically sensitive probe of the surface state, allowing us to separate the photoluminescence signal due to the protonation of ionizable defects at the surface of the flake from the adsorption of the hydrophobic alkyl groups of the organic solvent, which leads to localized emission at a distinct wavelength. Combining spectral SMLM with single-particle tracking allows us to reveal single excess proton trajectories as a succession of jumps between surface defects, mediated by the transport of the solvated proton charge along the solid/liquid interface. We evidence nontrivial dynamics for these interfacial charges, characterized at intermediate water fraction, by an increase in interfacial diffusivity due to a reduction of the

¹Laboratory of Nanoscale Biology, Institute of Bioengineering, School of Engineering, École Polytechnique Fédérale de Lausanne (EPFL), Lausanne, Switzerland. ²Laboratory of Soft Matter Science and Engineering, ESPCI Paris, PSL University, Sorbonne Université, CNRS, F-75005 Paris, France. ³Department of Mechanical Science and Engineering, University of Illinois at Urbana-Champaign, Champaign, IL, USA.

⁴School of Mathematics, Statistics and Physics, Newcastle University, Newcastle upon Tyne, NE1 7RU, UK. ⁵National Institute for Materials Science, Tsukuba, Japan. *Corresponding author. Email: jean.comtet@gmail.com

†Present address: Oden Institute for Computational Engineering and Sciences, Walker Department of Mechanical Engineering, The University of Texas at Austin, Austin, TX 78712, USA.

Aqueous and organic solvents activate distinct types of defects

Hosted at the surface of the flake, defects react strongly with their environment. As reported previously (26), a small density of active defects is observed in air (typically $\rho \approx 10^{-3}$ defects μm^{-2} frame $^{-1}$, with 20-ms exposure time). When the flakes are put in contact with solvents, the dynamics and density of activated defects increase markedly, pointing to the activation of defects by solvent molecules. Varying the solvent from aqueous to organic, we further observe that different solvents activate distinct types of defects. We compare in Fig. 1 (B and C) the spectral response of flakes in contact with water, where free protons H_3O^+ are present in solution (Fig. 1B) and with dodecane, an organic hydrocarbon solvent (Fig. 1C), showing drastically different emission spectra depending on these two conditions and pointing to the activation of distinct emission lines.

For the case of the hBN flake in contact with water (Fig. 1B), the ensemble spectra are characterized by an emission peak centered around $\lambda_A \approx 585$ nm (emission line A, green). Spectra from individual defects are shown in the inset. This emission line in hBN has been previously reported in a number of studies (26, 42, 44, 45). As represented in the green panel, we demonstrated in a previous report (26) that this emission line originates from defects in their protonated (acid) form, with the deprotonated (basic) defect being non-emissive. We attributed the emission to a protonated boron vacancy $V_B\text{H}$, with the on/off blinking behavior related to defect protonation/deprotonation through $V_B^- + \text{H}^+ \leftrightarrow V_B\text{H}$. Note that while our observations are fully consistent with an optical transition associated with distinct protonation states (26), the chemical nature associated with this emission line is still under debate.

Consistent with the absence of free protons in dodecane, emission line A is absent on flakes in contact with this organic solvent (Fig. 1C). We observe instead the activation of emitters at a second emission wavelength, centered here around $\lambda_B \approx 630$ nm (emission line B, red). This emission line has been reported previously in hBN (44, 46–48) and corresponds to the activation of a defect of unknown chemical structure, which we denote as D_2 . Anticipating the results below, this emission line is also observed for flakes in contact with other organic solvents (acetone, ethanol, and methanol), and we attribute this emission to the interaction of the defect with the non-polar hydrophobic alkyl groups of the organic solvent molecules. The dependence of this emission line on solvent polarity can be attributed to the interaction of the dipole of the defect in its excited state with the solvent (49) and is consistent with the slight observed redshift of the emission for increasing solvent polarity (fig. S6). The observation of such solvent-mediated activation of the emission should guide the identification of the chemical structure of the associated defect.

Interfacial adsorption and defect activity in binary aqueous solutions

Using the spectral signature of these emissive surface defects, we can probe how the physicochemical surface state of the hBN/liquid interface is affected by the presence of mixtures of water and amphiphilic organic solvents (methanol, ethanol, and acetone). We thus quantify the activity of defects under various proportions of water and organic solvents, characterized by the water volume fraction $X_{\text{H}_2\text{O}}$ [–]. We show, in Fig. 2A, colored superresolved maps

of active defects at the flake's surface, along with their ensemble spectra in the inset, and, in Fig. 2B, a reconstructed local spatial density map of activated defects on a $1\text{-}\mu\text{m}^2$ region at the surface of the flake (irrespective of defect spectral signature). Quantifying defect activity and spectral emission allows us to get a direct readout of the local chemical and charge state of surface defects as a function of bulk solvent composition, varying systematically the proportion of water and amphiphilic organic solvents in contact with the flake. As shown on the ensemble spectra in the insets of Fig. 2A, we observe, in all conditions, the presence of the $\lambda_A = 585$ nm green emission line, characterizing the presence of protonated boron vacancies (Fig. 1D). At low water content ($X_{\text{H}_2\text{O}} \leq 0.2$ in Fig. 2A), we observe the appearance of the second emission line $\lambda_B = 630$ nm, originating from the interaction of hydrophobic alkyl groups with surface defects D_2 . While the dense and random distribution of defects present at the flake's surface prevents us from cross-correlating the spatial distribution associated with each defect type, achieving better control of defect locations and densities might allow for such quantitative correlations.

To further characterize the variation of interfacial defect state with bulk solvent composition, we plot, in Fig. 2C, the fraction θ_A and θ_B of protonated and alkylated defects for decreasing water volume fraction $X_{\text{H}_2\text{O}}$ and, in Fig. 2D, their absolute density ρ_A and ρ_B (estimated as $\rho_i = \theta_i \cdot \rho_{\text{tot}}$, with ρ_{tot} being the total density of localized defects per frame). As quantified in Fig. 2C and schematically represented in Fig. 2D, the density of protonated boron vacancies ρ_A first increases with decreasing water content, from $7.10 \cdot 10^{-3}$ μm^{-2} frame $^{-1}$ s $^{-1}$ in pure water (Fig. 2E, i) to a maximum of $130.10 \cdot 10^{-3}$ μm^{-2} frame $^{-1}$ s $^{-1}$ in 60% water (Fig. 2E, ii), pointing to an increased surface affinity of proton charges to the hBN surface in these mixed solvent conditions. Further decreasing water content below $X_{\text{H}_2\text{O}} \leq 0.2$ leads to the activation of the second defect type D_2 due to the interaction with the hydrophobic alkyl groups of the organic solvent, as schematically represented in Fig. 2D. These observations are reported here for a mixture of water and acetone, but these trends are observed for the three organic solvents, with intrinsic variability when comparing individual flakes, due to local variation of the surface state (see fig. S5).

Spatiotemporal correlations and single proton charge tracking

Using the first type of defect as a marker for protonation events (Fig. 1B), we can then track and follow the dynamics of excess protons moving at the solid/liquid interface with single charge resolution. We restrict our analysis to the steady-state regime emerging under continuous illumination, where the surface concentration of active defects is constant (see fig. S4). Considering the condition $X_{\text{H}_2\text{O}} = 0.6$, we reconstruct, in Fig. 3A, a spatiotemporal plot of the activated defects in a $10\text{ }\mu\text{m}$ -by- $10\text{ }\mu\text{m}$ area, with localized defects color coded with increasing time along the vertical axis. Note that, in this particular condition, only protonated defects are active at the surface of the flake (Fig. 2B), such that defect activation is indeed solely due to the dynamics of proton charges.

As shown in Fig. 3A, we see clear correlations in the activation of nearby defects over successive frames. Some of these spatiotemporal trajectories are highlighted in red and shown in Fig. 3B. As defects are emissive in their protonated form, these trajectories correspond to the successive activation of nearby defects by a single excess proton hopping from defect to defect (26) and successively activating

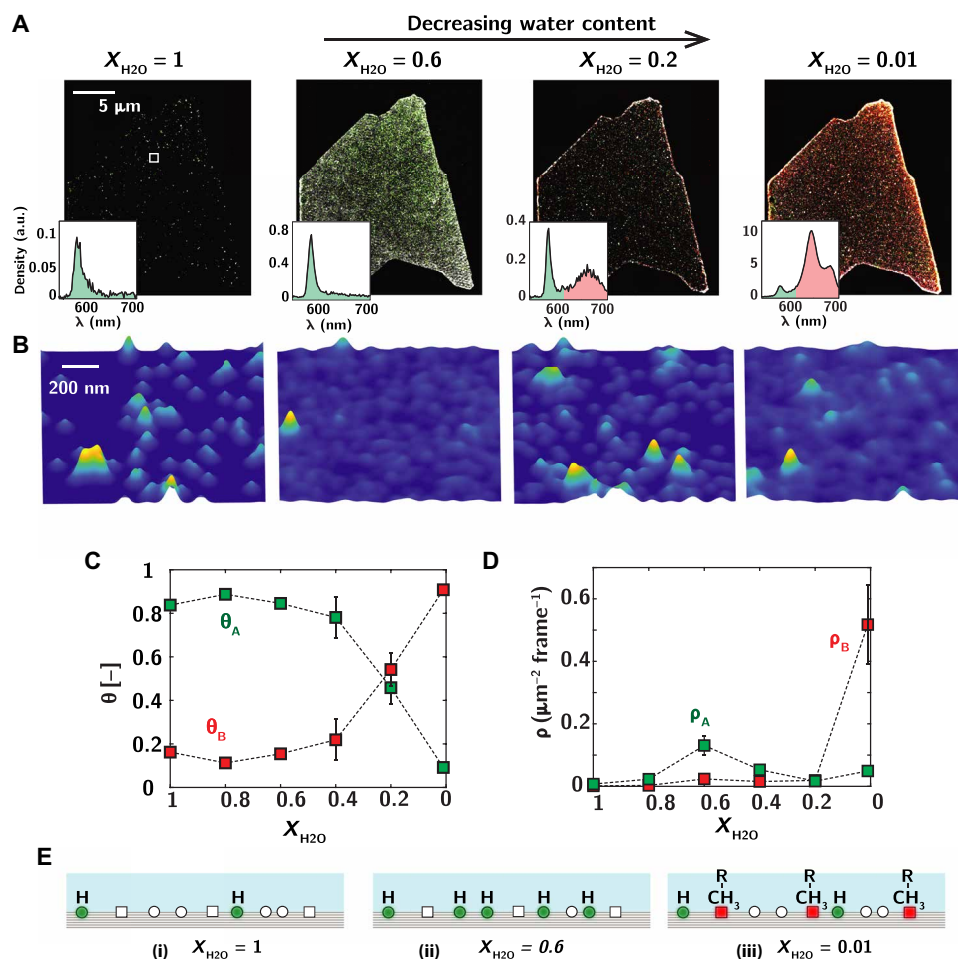


Fig. 2. Defect activity in binary mixtures. (A) Reconstructed images of emitters on flakes in binary solutions of water and organic solvents (here, water/acetone) at various volume fraction X_{H_2O} and with corresponding ensemble emission spectra in the insets. Defects with emission spectra λ_A and λ_B are represented in green and red, respectively. Defects with unassigned spectra are represented in white. The intensity scale for rendering defect density is the same in all conditions except for $X_{H_2O} = 0.01$, where the intensity scale is reduced by a factor of 10. (B) Zoom-in in the white box on the reconstructed images in (A) showing individual defect luminescence localization events irrespective of their emission spectra and rendered with fixed uncertainty of 20 nm. (C) Relative proportion of the spectral population $\theta_A = N_A/(N_A + N_B)$ and $\theta_B = 1 - \theta_A$ for decreasing water content. (D) Respective density ρ_A and ρ_B of active defects per frame for decreasing water content. Error bars in (C) and (D) correspond to the SD over two superresolved images reconstructed from 10,000 frames. Larger error bars at $X_{H_2O} = 0.4$ and 0.2 in (C) are due to the progressive increase of the number of alkylated defects over the two successive images. (E) Schematic of defect surface state in various solvent conditions.

the fluorescence signal. The fact that we can observe such correlated trajectories demonstrates that after desorbing from a defect, the solvated proton charge has a pronounced tendency to move along the solid/liquid interface, leading to the activation of a nearby defect site. This affinity of the solvated proton charge to the hBN solid surface is thus at the root of these observed spatiotemporal correlations.

DISCUSSION

Anomalous charge transport in mixtures

Analyzing charge trajectories for various bulk solvent composition, we highlight, in Fig. 4A, representative trajectories observed at the flake's surface for the three water volume fraction $X_{H_2O} = 1, 0.8,$ and 0.6 , showing that the relative proportion of water and organic solvent has a marked effect on interfacial charge dynamics at the

solid/liquid hBN interface. As we cannot attribute any spectra to low intensity defects (fig. S1), we track and follow activated defects indistinctively of their emission spectra. Down to $X_{H_2O} = 0.4$, these active emitters correspond solely to protonated defects (Fig. 2C, green), while for smaller water fraction, the localized emitters and the corresponding interfacial dynamics are characteristic of both protonated and alkylated defects.

Focusing first on the conditions for which only protonated defects are present at the surface of the flake, we plot, in Fig. 4B, the evolution of the mean square displacement $\text{MSD} = \langle (x(t) - x(0))^2 \rangle$ observed over all trajectories $x(t)$ (see the Supplementary Materials). From the initial increase of the MSD with time, we extract an effective surface diffusion coefficient D ($\text{m}^2 \text{s}^{-1}$) as $\text{MSD} \sim 4D \cdot t$, which we report in Fig. 4C for decreasing water fraction. As shown in this figure, we observe a 20-fold increase in D , from $D \approx 10^{-14} \text{ m}^2 \text{ s}^{-1}$ in pure aqueous solution to $D \approx 2.10^{-13} \text{ m}^2 \text{ s}^{-1}$ at intermediate water

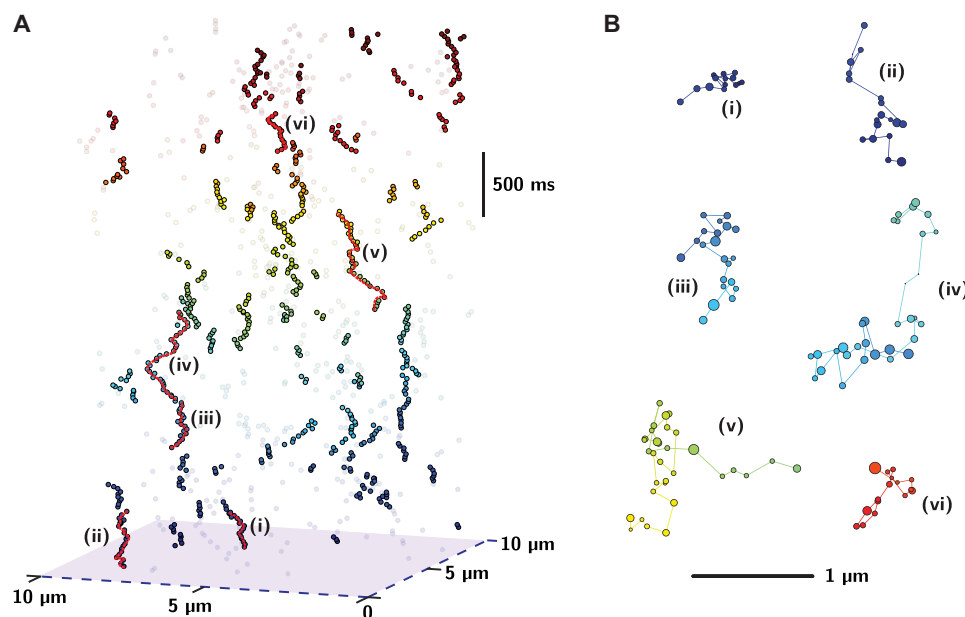


Fig. 3. Single-particle tracking of proton charge trajectories at the surface of hBN flake in binary solution ($X_{\text{H}_2\text{O}} = 0.6$). (A) Spatiotemporal trajectories of single proton charges observed over 4 s in a 10 μm -by-10 μm area over the hBN surface. The dimmer points correspond to uncorrelated blinking events. (B) Zoom-in over the spatiotemporal trajectories highlighted in (A). Localized defects are represented as dots, with the radius corresponding to the localization uncertainty.

fraction ($X_{\text{H}_2\text{O}} = 0.6$). The diffusion coefficient further decreases when reaching lower fraction of water (note that in the conditions of low water fraction $X_{\text{H}_2\text{O}} < 0.4$, the effective diffusion coefficient and observed time traces would characterize interfacial mobility of both water and organic solvent molecules). This measured value $D \approx 10^{-13}$ to 10^{-14} $\text{m}^2 \text{s}^{-1}$ for the interfacial proton diffusion coefficient is five to six orders of magnitude lower than the bulk proton diffusion coefficient $D_{\text{bulk}} \approx 10^{-8}$ $\text{m}^2 \text{s}^{-1}$, consistent with a surface transport limited by the desorption of proton charges out of the defects (26). Expressing the surface diffusion coefficient D , as an activated desorption-limited process, we can write $D \sim \frac{1}{4} \nu_0 \cdot a^2 \cdot e^{-\Delta F_{\text{defect}}/kT}$, with $\nu_0 \approx 1$ GHz being a characteristic attempt frequency, $a \approx 10$ to 100 nm being a characteristic interdefect distance, and ΔF_{defect} (eV) being a free energy desorption barrier. The 20-fold increase in interfacial mobility at intermediate water concentration would then correspond to a net decrease of the desorption barrier by $3 k_B T$ or 77 meV. In pure water, taking $D \approx 10^{-14}$ $\text{m}^2 \text{s}^{-1}$, the mean desorption free energy is estimated to be of the order of 0.4 to 0.5 eV.

Elementary steps during proton surface transport

Because we can access the details of the trajectories at the single-molecule scale, we are able to further investigate interfacial proton charge dynamics. We can thus disentangle the various elementary steps at play during proton surface transport, i.e., the desorption of the proton out of the defect site, the transport of the solvated proton charge along the solid/liquid interface to the next defect, and the irreversible desorption of the proton out in the bulk. Analyzing these random walks, we extract, in Fig. 4 (D and E), both the residence time at each defect site (merging uncertainty-limited localizations as one site) and the number of visited defects along a single trajectory (see the Supplementary Materials).

We first show, in Fig. 4D, the distribution of residence time on the defects when the flake is in contact with aqueous solutions (blue, $X_{\text{H}_2\text{O}} = 1$) and at intermediate water fraction (green, $X_{\text{H}_2\text{O}} = 0.6$). These distributions follow power law scaling (dashed lines with slope -2 and -3.8), and we observe a steeper distribution of residence time for $X_{\text{H}_2\text{O}} = 0.6$ (comparing green and blue curves), consistent with the fact that the increase in the effective surface diffusion observed at intermediate water concentration is due to the facilitated proton desorption out of the defects, leading to a reduced residence time on the defect sites.

A major observation relates to the correlation in the activation of adjacent defect sites, demonstrating the affinity of the solvated proton charge to the solid/liquid interface. To analyze this effect in more detail, we plot, in Fig. 4E, the distribution of the number of defects visited during a single trajectory for various water fractions. The number of visited defects is distributed approximately exponentially and follows the same nonmonotonic trend as the diffusion coefficient, with a maximum in the number of visited defects at intermediate water fraction (Fig. 4E, green). These observations are consistent with the large and homogenous activation of defects observed at the flake's surface at intermediate water fraction (Fig. 2, A and B) and indicate an increased affinity of the proton charges to the solid surface due to either an increased affinity of the solvated charge to the pristine surface during the transport between adjacent defects or an increased probability of readsorption to the surrounding surface defects. Last, at low water fraction, the number of visited defects decreases, which would indicate an altered interaction of the proton with the defect-free part of the crystal. Note, however, that in these conditions, another type of defect is also active at the surface because of hydrophobic interaction with the solvent, making the distinction of the dynamics between protonated and alkylated defects difficult.

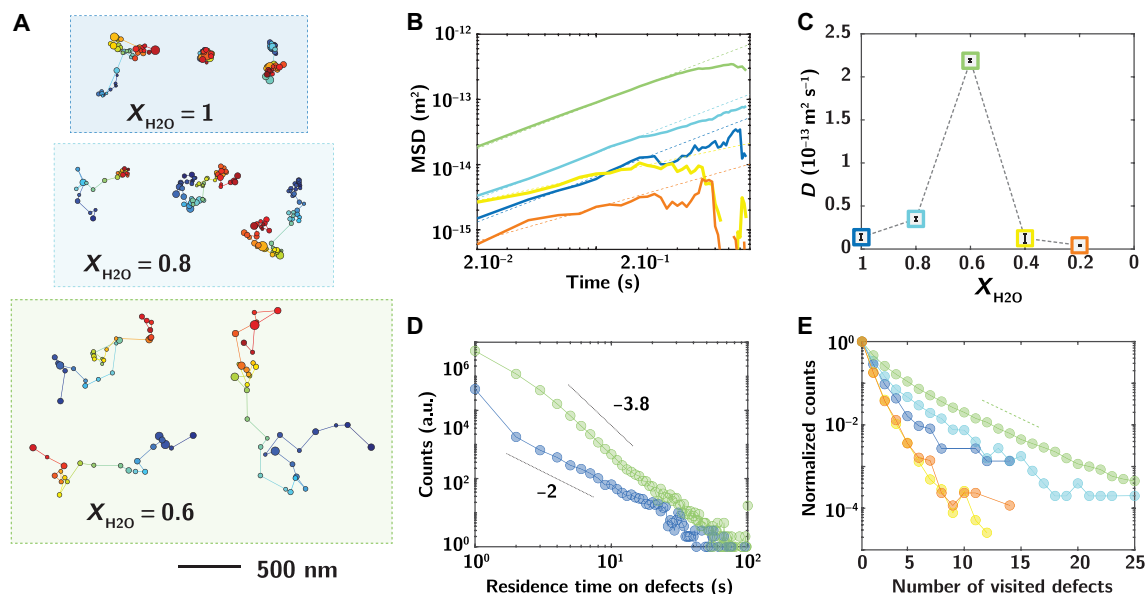


Fig. 4. Anomalous interfacial charge transport. (A) Sample trajectories for various water volume fraction $X_{\text{H}_2\text{O}}$ (in water/acetone mixture). Localized defects are represented as dots, with the radius corresponding to the localization uncertainty. (B) Evolution of the MSD with time for various water volume fraction $X_{\text{H}_2\text{O}}$. Green, light blue, dark blue, yellow, and orange correspond to $X_{\text{H}_2\text{O}}=1, 0.8, 0.6, 0.4,$ and $0.2,$ respectively. (C) Variation of the diffusion coefficient with water volume fraction $X_{\text{H}_2\text{O}}$. (D) Distribution of the residence time on defects for $X_{\text{H}_2\text{O}} = 1$ (blue) and $X_{\text{H}_2\text{O}} = 0.6$ (green). (E) Distribution of the number N of defect sites visited by individual trajectories for varying water fraction. The green dashed line characterizes the exponential decay $\sim e^{-N/N_1}$ with $N_1 \approx 3.3$.

To analyze more quantitatively this segregation of the proton charges at the interface, we follow previous ensemble observations (50, 51) and assume the presence of a free energy barrier ΔG (eV) responsible for the trapping of the solvated proton charge at the interface between the hBN and the solvent during transport between adjacent defects. The presence of this barrier would lead to a characteristic time scale $\tau_{\text{escape}} \sim 1/\nu_1 \cdot e^{\Delta G/kT}$ for the escape of the solvated proton out of the pristine interface, with $\nu_1 \approx 10^{15} \text{ s}^{-1}$ being the typical frequency for rate processes at surfaces (50). Assuming that the proton diffuses from one defect to the other following a bidimensional random walk with a diffusion coefficient of the order of its bulk value $D_{\text{bulk}} \approx 10^{-8} \text{ m}^2 \text{ s}^{-1}$, we can also express the characteristic time for transport between adjacent sites as $\tau_{\text{diff}} \sim a^2/4D_{\text{bulk}} \approx 2.5$ to 250 ns , with $a \approx 10$ to 100 nm being the characteristic inter-defect distance. The distribution in the number N of defects visited by individual protons can then be expressed as $P(N) \sim e^{-N/N_1}$, with $N_1 \approx \tau_{\text{escape}}/\tau_{\text{diff}}$. For $X_{\text{H}_2\text{O}} = 0.6$, we estimate $N_1 \approx 3.3$ (Fig. 4E), and the associated free energy barrier ΔG can then be expressed as $\Delta G = kT \cdot \log\left(\frac{a^2 \nu_1}{4D_{\text{bulk}}} \cdot N_1\right) \approx 11$ to $16 \text{ kT} \approx 0.3$ to 0.4 eV . Although coarse, this estimation is in fair agreement with the free energy barrier for proton trapping at pristine interfaces obtained from simulations, ranging from 0.15 to 0.3 eV (fig. S10). Note, however, that our simulations rather show a monotonic decrease of the affinity of the proton charge to the pristine surface for decreasing water content.

Simulation

To probe mechanistically the kinetic factors affecting proton charge dynamics, we turn in Fig. 5 to ab initio simulations of the reactivity of the negatively charged boron vacancies. We show, in Fig. 5A, the simulation cell composed of a mixture of water and methanol molecules interacting with the hBN surface. Water/methanol mixture was considered for the simulations, as methanol represents the

simplest organic chemical species having an amphiphilic character due to its hydrophobic $-\text{CH}_3$ and its hydrophilic $-\text{OH}$ and is thus a good model system to understand the behavior of potentially more complex water/ethanol and water/acetone mixtures.

As shown in Fig. 5B, we compute the energy barrier for the transfer of proton from the H_3O^+ cation to the negatively charged boron vacancy V_{B}^- (see the Supplementary Materials). Varying, as shown in Fig. 5C, the first solvation shell of the hydronium from (i) two water, (ii) one water and one methanol, to (iii) two methanol molecules, we extract from these simulations the enthalpic desorption energy barrier for defects in the ground state (blue, ΔE_{GS}) and excited state (red, ΔE_{ES}), respectively.

As reported in Fig. 5C, our simulations evidence a reduction of the enthalpic energy desorption barrier ΔE_{GS} and ΔE_{ES} by ~ 120 and $\sim 200 \text{ meV}$, respectively, when a single methanol molecule is present in the hydronium solvation shell, in qualitative agreement with the large increase in diffusion coefficient observed in Fig. 4C at intermediate water concentration. Note that the total free energy barrier ΔF_{GS} for proton desorption will be further reduced by a constant entropic contribution of -0.5 eV in the three conditions (i to iii) and might further decrease in mixture because of their anomalous mixing entropy (see the Supplementary Materials) (52). On the contrary, the free energy barrier for proton adsorption shows a smaller increase of 40 to 120 meV at intermediate water concentration (see the Supplementary Materials), which would suggest that the increased number of visited defects evidenced in Fig. 4E is indeed due to an enhanced affinity of the solvated charge to the solid surface rather than an increased readsorption probability at the defect site.

To interpret mechanistically this change in the desorption barrier out of the defect, we analyzed the charge density of the solvating molecules for the various compositions of the solvation shells (fig. S9). We observe that when methanol is present in the first solvation shell of the hydronium ion, its large electron cloud leads to an

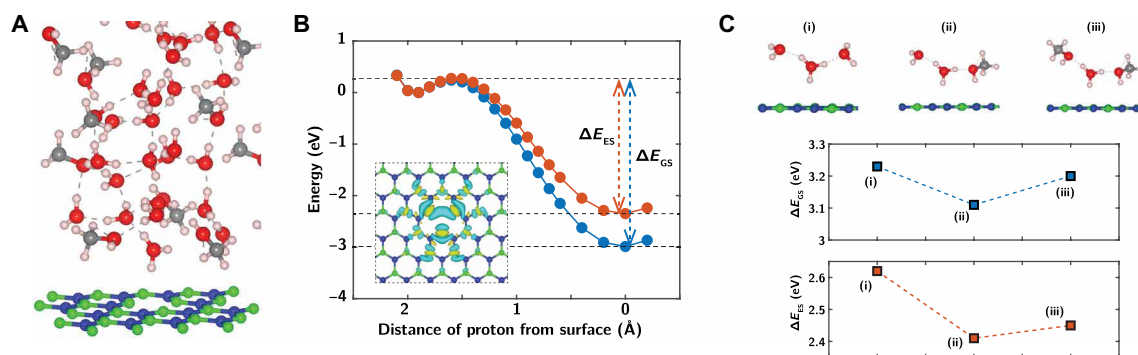


Fig. 5. Simulation of defect reactivity in binary mixtures. (A) Simulation setup of a 50% water-methanol mixture on hBN. Oxygen is shown in red. Hydrogen is shown in white. Carbon is shown in teal. Boron is shown in brown, and nitrogen is shown in dark blue. The gray dashed lines represent the hydrogen bonds between oxygen and hydrogen atoms. (B) Energy barriers for a proton reacting with the negatively charged boron vacancy V_B^- in a 50% mixture of methanol and water with one water and one methanol molecule in the first solvation shells of the hydronium ion near the defect as shown in (A). Blue: Defect in the ground state. Red: Defect in the excited state. The desorption energy barrier is shown as ΔE . The inset further shows the difference in the electron density between the excited and the ground state (blue indicates a positive value of charge density difference and yellow indicates a negative charge density difference). (C) Desorption energy barrier ΔE_{GS} and ΔE_{ES} for a defect in ground state and excited state, respectively, with different molecules in the first solvation shell of the hydronium ion. (i) Two water molecules; (ii) one water and one methanol molecule; (iii) two methanol molecules.

increase in the electron density on the central oxygen of the aqueous core of the hydronium ion, rationalizing the observed decrease in the desorption barrier of H^+ at intermediate water concentration. This effect is consistent with previous analysis (38).

Comparing desorption energy for defects in the ground state and excited state, respectively (Fig. 5, B and C, comparing red and blue), we also find a 0.6 eV reduction of the desorption energy barrier for a defect in the excited state, consistent with our experimental observations that proton dissociation is favored under illumination (fig. S4) (26). The inset of Fig. 5B shows the difference in electron density between the excited and the ground state, evidencing a positive charge density difference around the defect in its excited state, consistent with a higher electrostatic repulsion leading to a net decrease of the desorption barrier. However, note that a quantitative agreement between the absolute computed desorption energy barrier and our experimentally measured diffusion coefficient is out of reach of these simulations. This could be due to either an incorrect defect type, with a less electro-negative defect that would indeed decrease the desorption barrier, or the fact that photoexcitation could lead to an excited state with higher energy, distinct from the one considered in this simulation.

Applying spectral SMLM to defected hBN crystals in contact with binary mixtures of water and organic solvents, we investigated, at the single proton scale, the complex relationship between solvation and charge dynamics at solid/liquid interfaces. We evidenced a nontrivial dynamics of interfacial proton charges with solvent content, characterized at intermediate water concentration by an increased interfacial diffusivity due to a reduced desorption energy barrier of the charge out of the defects, concomitant with an increased affinity of the charge to the solid surface. Our measurements, corroborated by *ab initio* simulations, demonstrate the subtle role of solvation on interfacial proton charge dynamics and further establish the potential of SMLM for the investigation of a wide range of dynamic processes at solid/liquid interfaces.

MATERIALS AND METHODS

Spectral SMLM setup and imaging conditions

Imaging was performed using a home-built spectral SMLM setup described previously (42). Briefly, the sample is excited using a

561-nm laser (Monolithic Laser Combiner 400B, Agilent Technologies). The excitation beam from the laser is focused on the back focal plane of an oil-immersion 100× objective (Olympus TIRFM 100X, 1.45 NA), leading to the wide-field illumination of the sample. Photoluminescence signal from the sample is collected by the same objective and filtered using dichroic and emission filters (ZT488/561rpc-UF1 and ZET488/561m, Chroma). Emission is further split in two “spatial” and “spectral” paths using a beam splitter. As described in (53), these two paths consist of two telescopes, sharing one lens and with a magnification factor of 1.6 and 1.4, respectively. Lenses are achromatic doublet lenses (Qioptiq). A prism (PS863, Thorlabs) is placed in the spectral path at the Fourier plane and at the angle of minimum deviation. Spatial and spectral images of the sample are then projected on an EMCCD camera (Andor iXon Life 897), with a back projected pixel size of 100 nm in the spatial channel. In the spectral channel, the prism leads to a vertical shift and dispersion of the emitter position equal to 0.25 pixel/nm. The camera is operated with an electron-multiplying gain of 150 and sampling time of 20 ms. Illumination power, as measured at the back focal plane of the objective, is set to 44 or 60 mW, corresponding to power densities of 2.2 to 3 kW cm⁻². The sample is mounted on a piezoelectric scanner (Nano-Drive, Mad City Labs) to compensate for vertical drift using an infrared-based feedback loop.

Sample preparation and buffer solutions

hBN multilayer flakes are exfoliated from high-quality bulk crystals (41) on glass coverslips (#1.5 micro cover glass; 25 mm in diameter; Electron Microscopy Sciences). Homogeneous distribution of defects at the surface of the flake are induced by submitting the flake to a low-power oxygen plasma treatment [100 mW, 30 sccm (standard cubic centimeters per minute) O₂ flow] ranging from 10 to 60 s.

Binary solvent mixtures are obtained by mixing deionized (DI) water (pH 5.5) with methanol (99.8% purity; Sigma-Aldrich), ethanol (99% purity; Sigma-Aldrich), and acetone (99.5% purity; Sigma-Aldrich). Experiments in pure aqueous solutions were carried out using either DI water (pH 5.5) or water solutions buffered with 100 mM KCl at pH 3 (adjusted using HCl). Upon interaction of the hBN flakes with concentrated or pure solutions of organic solvent, we

observe irreversible change of the surface state (the original state is not recovered when going back to pure water) and slow aging (fig. S1). Experiments in binary mixtures at various water volume fraction are thus performed by progressively increasing the concentration of organic solvent in the mixtures.

SMLM data analysis

Emitters in the spatial channels and peak emission spectra in the spectral channels are localized using the ImageJ plugin Thunder-STORM (54). Briefly, a wavelet filter is applied to each frame. Peaks are then fitted by two-dimensional integrated Gaussians. In the spatial channel, only emitters with intensity larger than the SD of the first wavelet level are considered. This localization procedure allows us to obtain localization tables for the spatial positions of active emitters at the surface of the flake at each time frame. Localization precision $\sigma_{x,y}$ for least square estimate is calculated on the basis of the Thompson-Larson-Webb formula (55). The leading order in localization precision scales as $\sigma_{x,y} = \sigma_{\text{PSF}}/\sqrt{N}$, where $\sigma_{\text{PSF}} \approx 150$ nm is the SD of the Gaussian fit of emitter's intensity (corresponding to a diffraction-limited spot fixed by the point spread function with a full width at half maximum of ~ 350 nm) and N is the number of photons emitted by the defect during the acquisition of one frame. We obtain an average localization precision around 20 nm.

Spectral assignment of emitters in the spatial channel is obtained by computing the projected position of emitters in the spectral channel for a fixed emission wavelength of 650 nm and performing a pair-search algorithm to find the closest spectral peak localization in a vertically elongated rectangular zone around their image. Full spectra in Fig. 1 are obtained by averaging the spectrum of single emitters over all frames for which spectral assignment is successful. As shown in fig. S2, the spectra of individual defects are obtained preferentially for the brighter surface defects.

Trajectory analysis

Charge trajectories at the surface of the flake were analyzed using single-particle tracking techniques as described in a previous work (26) using the available online tracking algorithm (<http://site.physics.georgetown.edu/matlab/>). Briefly, emitters are first localized as described above. Active sites are then identified as belonging to the same trajectory when present in two consecutive frames within a user-defined threshold distance $d \approx 300$ nm [unambiguously defined from the distribution of step length δl ; see (26)]. For most conditions, this threshold is small compared to the typical distance between active sites on a single frame, allowing to consistently extract the trajectories. When the surface concentration of active sites becomes too large (typically larger than $0.5 \mu\text{m}^{-2}$ frame $^{-1}$, leading to an average interdefect distance of 0.8 μm), spurious correlations between nearby sites lead to false trajectory assignment, and we discard these conditions.

The ensemble diffusion coefficient is then obtained through a linear fit of the initial increase of the MSD with time (26). This MSD can be computed by restricting the average on trajectories larger than a threshold length N_L . For low density of defects and large diffusion coefficient, the obtained MSD is independent of this threshold trajectory length. In the opposite conditions of low diffusion coefficient and large defect density, spurious correlations between randomly activating defects lead to an overestimation of the MSD at short times [see (26)]. For consistency in our analysis, we thus systematically compute the MSD with $10 \leq N_L \leq 15$ and report the variation

in the measured diffusion coefficient over this range of threshold length as error bars.

To obtain the distribution of residence time on each defect site (Fig. 4D) and the number of defects visited along a given trajectory (Fig. 4E), successive localizations along the trajectories are merged when they are within a defined distance corresponding to twice their localization uncertainty.

Simulation

The barrier calculations are performed by a self-consistent analysis of the density functional theory (DFT) (56) using the Vienna ab initio simulation (VASP) package (57, 58). The Perdew-Burke-Ernzerhof (PBE) exchange-correlation functional (59), which comes under the generalized gradient approximation (GGA), was used, and projected augmented wave pseudopotentials with a 400-eV energy cutoff and Gamma point-centered k-point of $4 \times 4 \times 4$ were used. The barrier for H_3O^+ and V_B^- -hBN is calculated by slowly moving the proton away from the water molecule and toward the surface with the system shown in Fig. 5A. Each unit cell consists of 42 molecules of H_2O and 1 molecule of H_3O^+ placed on an hBN surface with a negatively charged boron vacancy (V_B^-). The simulation box has dimensions of 10.0182 Å by 8.676 Å by 30 Å. In the simulations of mixtures, an additional 20 molecules of methanol are added to the system to ensure a 50% by volume mixture of methanol-water. All the structures are relaxed using an energy convergence criterion of 10^{-8} eV. The entropic barriers are calculated using standard statistical mechanics (60) and are independent of the molecules in the first coordination shell (see the Supplementary Materials).

For calculating the energy barrier in the excited state, the band energy diagram of a boron vacancy on hBN is first evaluated from the eigenvalues of the ground state in VASP using the PBE potential. Next, the occupancies of the electrons in the excited state are set using the constrained GGA approach (61). The occupancies are set in such a way that one electron is excited to its first excited state (defect state 1 in fig. S7). Last, the self-consistent calculations are repeated to calculate the static energy barriers for the excited state with the same procedure as the barrier calculations of the ground state.

To study the interfacial free energy profile of a hydronium ion in water-methanol mixtures, molecular dynamics simulations were performed using LAMMPS (62) for pure water, methanol, and 50% methanol-water mixture. The free energies were obtained from the potential of mean force and through umbrella sampling of multiple simulations. The system consists of 128 atoms on the hBN surface and 1 H_3O^+ molecule, with the pure water system having 344 water molecules, pure methanol having 160 methanol molecules, and 50% methanol system having 178 water and 80 methanol molecules. The liquid mixtures are placed on the hBN surface, with the dimension of the simulation box being 20.036364 Å by 17.352 Å by 80 Å and a canonical ensemble is used at 300 K. The Lennard-Jones parameters used for B, N, and O in the molecular dynamics simulations have been taken from (63), and C–C interactions were taken from (64). The remaining interactions were estimated through the Lorentz-Berthelot mixing rules. The bonding parameters for water and methanol were taken from SPC/E (65) and OPLS/AA (66) potential models of water and methanol, respectively. The simulations for fig. S10 are equilibrated for 2 ns, and the data are collected in the production run of 5 ns.

SUPPLEMENTARY MATERIALS

Supplementary material for this article is available at <https://science.org/doi/10.1126/sciadv.abg8568>

REFERENCES AND NOTES

1. M. Bränden, T. Sanden, P. Brzezinski, J. Widengren, Localized proton microcircuits at the biological membrane–water interface. *Proc. Natl. Acad. Sci. U.S.A.* **103**, 19766–19770 (2006).
2. S. Serowy, S. M. Saparov, Y. N. Antonenko, W. Kozlovsky, V. Hagen, P. Pohl, Structural proton diffusion along lipid bilayers. *Biophys. J.* **84**, 1031–1037 (2003).
3. K. Gopinadhan, S. Hu, A. Esfandiari, M. Lozada-Hidalgo, F. C. Wang, Q. Yang, A. V. Tyurnina, A. Keerthi, B. Radha, A. K. Geim, Complete steric exclusion of ions and proton transport through confined monolayer water. *Science* **363**, 145–148 (2019).
4. K. G. Zhou, K. S. Vasu, C. T. Cherian, M. Neek-Amal, J. C. Zhang, H. Ghorbanfekr-Kalashami, K. Huang, O. P. Marshall, V. G. Kravets, J. Abraham, Y. Su, A. N. Grigorenko, A. Pratt, A. K. Geim, F. M. Peeters, K. S. Novoselov, R. R. Nair, Electrically controlled water permeation through graphene oxide membranes. *Nature* **559**, 236–240 (2018).
5. Z. Zhang, X. Li, J. Yin, Y. Xu, W. Fei, M. Xue, Q. Wang, J. Zhou, W. Guo, Emerging hydrovoltaic technology. *Nat. Nanotechnol.* **13**, 1109–1119 (2018).
6. A. Siria, M. L. Bocquet, L. Bocquet, New avenues for the large-scale harvesting of blue energy. *Nat. Rev. Chem.* **1**, 0091 (2017).
7. X. Qian, L. Chen, L. Yin, Z. Liu, S. Pei, F. Li, G. Hou, S. Chen, L. Song, K. H. Thebo, H.-M. Cheng, W. Ren, CdPS 3 nanosheets-based membrane with high proton conductivity enabled by Cd vacancies. *Science* **370**, 596–600 (2020).
8. A. Michaelides, P. Hu, Catalytic water formation on platinum: A first-principles study. *J. Am. Chem. Soc.* **123**, 4235–4242 (2001).
9. W. Karim, C. Spreafico, A. Kleibert, J. Gobrecht, J. Vandevondele, Y. Ekinci, J. A. Van Bokhoven, Catalyst support effects on hydrogen spillover. *Nature* **541**, 68–71 (2017).
10. W. Schmickler, E. Santos, *Interfacial Electrochemistry* (Springer, 2010), pp. 1–272.
11. M. Kühne, F. Börmert, S. Fecher, M. Ghorbani-Asl, J. Biskupek, D. Samuëlis, A. V. Krasheninnikov, U. Kaiser, J. H. Smet, Reversible superdense ordering of lithium between two graphene sheets. *Nature* **564**, 234–239 (2018).
12. I. Siretanu, D. Ebeling, M. P. Andersson, S. L. S. Stipp, A. Phillippe, M. C. Stuart, D. Van Den Ende, F. Mugele, Direct observation of ionic structure at solid-liquid interfaces: A deep look into the stern layer. *Sci. Rep.* **4**, 19–21 (2014).
13. F. Mugele, B. Bera, A. Cavalli, I. Siretanu, A. Maestro, M. Duits, M. Cohen-Stuart, D. Van Den Ende, I. Stocker, I. Collins, Ion adsorption-induced wetting transition in oil-water-mineral systems. *Sci. Rep.* **5**, 1–8 (2015).
14. D. Ebeling, D. van den Ende, F. Mugele, Electrostatic interaction forces in aqueous salt solutions of variable concentration and valency. *Nanotechnology* **22**, 305706 (2011).
15. S. R. Van Lin, K. K. Grotz, I. Siretanu, N. Schwierz, F. Mugele, Ion-specific and pH-dependent hydration of mica-electrolyte interfaces. *Langmuir* **35**, 5737–5745 (2019).
16. D. P. Hoogerheide, S. Garaj, J. A. Golovchenko, Probing surface charge fluctuations with solid-state nanopores. *Phys. Rev. Lett.* **102**, 5–8 (2009).
17. E. Secchi, A. Niguès, L. Jubin, A. Siria, L. Bocquet, Scaling behavior for ionic transport and its fluctuations in individual carbon nanotubes. *Phys. Rev. Lett.* **116**, 1–5 (2016).
18. O. B. Tarun, C. Hanneschläger, P. Pohl, S. Roke, Label-free and charge-sensitive dynamic imaging of lipid membrane hydration on millisecond time scales. *Proc. Natl. Acad. Sci. U.S.A.* **115**, 201719347 (2018).
19. D. Lis, E. H. G. Backus, J. Hunger, S. H. Parekh, M. Bonn, Liquid flow along a solid surface reversibly alters interfacial chemistry. *Science* **344**, 1138–1142 (2014).
20. P. Ober, W. Q. Boon, M. Dijkstra, E. H. G. Backus, R. Van Roij, M. Bonn, Liquid flow reversibly creates a macroscopic surface charge gradient. *Nat. Commun.* **12**, 4102 (2020).
21. M. Ricci, P. Spijker, K. Voitchovsky, Water-induced correlation between single ions imaged at the solid-liquid interface. *Nat. Commun.* **5**, 4400 (2014).
22. N. Amdursky, Y. Lin, N. Aho, G. Groenhof, Exploring fast proton transfer events associated with lateral proton diffusion on the surface of membranes. *Proc. Natl. Acad. Sci. U.S.A.* **116**, 2443–2451 (2019).
23. D. A. Cherepanov, P. Pohl, V. Hagen, Y. N. Antonenko, A. Springer, Protons migrate along interfacial water without significant contributions from jumps between ionizable groups on the membrane surface. *Proc. Natl. Acad. Sci. U.S.A.* **108**, 14461–14466 (2011).
24. T. Mouterde, L. Bocquet, Interfacial transport with mobile surface charges and consequences for ionic transport in carbon nanotubes. *Eur. Phys. J. E* **41**, 148 (2018).
25. B. L. Werkhoven, J. C. Everts, S. Samin, R. Van Roij, Flow-induced surface charge heterogeneity in electrokinetics due to stern-layer conductance coupled to reaction kinetics. *Phys. Rev. Lett.* **120**, 264502 (2018).
26. J. Comtet, B. Grosjean, E. Glushkov, A. Avsar, K. Watanabe, T. Taniguchi, R. Vuilleumier, M.-L. L. Bocquet, A. Radenovic, Direct observation of water-mediated single-proton transport between hBN surface defects. *Nat. Nanotechnol.* **15**, 598–604 (2020).
27. S. Stehle, A. S. Braeuer, Hydrogen bond networks in binary mixtures of water and organic solvents. *J. Phys. Chem. B* **123**, 4425–4433 (2019).
28. L. Dougan, S. P. Bates, R. Hargreaves, J. P. Fox, J. Crain, J. L. Finney, V. Réat, A. K. Soper, Methanol-water solutions: A bi-percolating liquid mixture. *J. Chem. Phys.* **121**, 6456–6462 (2004).
29. M. Nagasaka, K. Mochizuki, V. Leloup, N. Kosugi, Local structures of methanol-water binary solutions studied by soft x-ray absorption spectroscopy. *J. Phys. Chem. B* **118**, 4388–4396 (2014).
30. S. Dixit, J. Crain, W. C. K. Poon, J. L. Finney, A. K. Soper, Molecular segregation observed in a concentrated alcohol-water solution. *Nature* **416**, 829–832 (2002).
31. J. A. Batista da Silva, F. G. B. Moreira, V. M. Leite dos Santos, R. L. Longo, On the hydrogen bond networks in the water-methanol mixtures: Topology, percolation and small-world. *Phys. Chem. Chem. Phys.* **13**, 6452–6461 (2011).
32. O. Björneholm, M. H. Hansen, A. Hodgson, L. M. Liu, D. T. Limmer, A. Michaelides, P. Pedevilla, J. Rossmels, H. Shen, G. Tocci, E. Tyrode, M. M. Walz, J. Werner, H. Bluhm, Water at interfaces. *Chem. Rev.* **116**, 7698–7726 (2016).
33. R. Gupta, A. Chandra, An ab initio molecular dynamics study of diffusion, orientational relaxation and hydrogen bond dynamics in acetone-water mixtures. *J. Mol. Liq.* **165**, 1–6 (2012).
34. S. Y. Noskov, G. Lamoureux, B. Roux, Molecular dynamics study of hydration in ethanol-water mixtures using a polarizable force field. *J. Phys. Chem. B* **109**, 6705–6713 (2005).
35. R. Semino, J. Martí, E. Guàrdia, D. Laria, Excess protons in mesoscopic water-acetone nanoclusters. *J. Chem. Phys.* **137**, 194301 (2012).
36. J. A. Morrone, K. E. Haslinger, M. E. Tuckerman, Ab initio molecular dynamics simulation of the structure and proton transport dynamics of methanol-water solutions. *J. Phys. Chem. B* **110**, 3712–3720 (2006).
37. R. Semino, M. P. Longinotti, Excess protons in water-acetone mixtures. II. A conductivity study. *J. Chem. Phys.* **139**, 164510 (2013).
38. M. K. Petersen, G. A. Voth, Amphiphilic character of the hydrated proton in methanol-water solutions. *J. Phys. Chem. B* **110**, 7085–7089 (2006).
39. K. Voitchovsky, D. Giofrè, J. J. Segura, F. Stellacci, M. Ceriotti, Thermally-nucleated self-assembly of water and alcohol into stable structures at hydrophobic interfaces. *Nat. Commun.* **7**, 13064 (2016).
40. Y. F. Yano, Correlation between surface and bulk structures of alcohol-water mixtures. *J. Colloid Interface Sci.* **284**, 255–259 (2005).
41. T. Taniguchi, K. Watanabe, Synthesis of high-purity boron nitride single crystals under high pressure by using Ba-BN solvent. *J. Cryst. Growth* **303**, 525–529 (2007).
42. J. Comtet, E. Glushkov, V. Navikas, J. Feng, V. Babenko, S. Hofmann, K. Watanabe, T. Taniguchi, A. Radenovic, Wide-field spectral super-resolution mapping of optically active defects in hexagonal boron nitride. *Nano Lett.* **19**, 2516–2523 (2019).
43. J. Feng, H. Deschout, S. Caneva, I. Lon, P. Lazić, A. Radenovic, S. Hofmann, I. Lončarić, P. Lazić, A. Radenovic, Imaging of optically active defects with nanometer resolution. *Nano Lett.* **18**, 1739–1744 (2018).
44. L. J. Martínez, T. Pelini, V. Waselowski, J. R. Maze, B. Gil, G. Cassabois, V. Jacques, Efficient single photon emission from a high-purity hexagonal boron nitride crystal. *Phys. Rev. B* **94**, 121405 (2016).
45. G. Grosso, H. Moon, B. Lienhard, S. Ali, D. K. Efetov, M. M. Furchi, P. Jarillo-Herrero, M. J. Ford, I. Aharonovich, D. Englund, Tunable and high-purity room temperature single-photon emission from atomic defects in hexagonal boron nitride. *Nat. Commun.* **8**, 705 (2017).
46. F. Hayee, L. Yu, J. L. Zhang, C. J. Ciccarino, M. Nguyen, A. F. Marshall, I. Aharonovich, J. Vučković, P. Narang, T. F. Heinz, J. A. Dionne, Revealing multiple classes of stable quantum emitters in hexagonal boron nitride with correlated optical and electron microscopy. *Nat. Mater.* **19**, 534–539 (2020).
47. S. Choi, T. T. Tran, C. Elbadawi, C. Lobo, X. Wang, S. Juodkazis, G. Seniutinas, M. Toth, I. Aharonovich, Engineering and localization of quantum emitters in large hexagonal boron nitride layers. *ACS Appl. Mater. Interfaces* **8**, 29642–29648 (2016).
48. T. T. Tran, C. Elbadawi, D. Totonjian, C. J. Lobo, G. Grosso, H. Moon, D. R. Englund, M. J. Ford, I. Aharonovich, M. Toth, Robust multicolor single photon emission from point defects in hexagonal boron nitride. *ACS Nano* **10**, 7331–7338 (2016).
49. A. S. Klymchenko, Solvatochromic and fluorogenic dyes as environment-sensitive probes: Design and biological applications. *Acc. Chem. Res.* **50**, 366–375 (2017).
50. E. Weichselbaum, M. Österbauer, D. G. Knyazev, O. V. Batishev, S. A. Akimov, T. Hai Nguyen, C. Zhang, G. Knör, N. Agmon, P. Carloni, P. Pohl, Origin of proton affinity to membrane/water interfaces. *Sci. Rep.* **7**, 4553 (2017).
51. C. Zhang, D. G. Knyazev, P. Carloni, T. H. Nguyen, P. Pohl, E. Ippoliti, Y. A. Vereshaga, Water at hydrophobic interfaces delays proton surface-to-bulk transfer and provides a pathway for lateral proton diffusion. *Proc. Natl. Acad. Sci. U.S.A.* **109**, 9744–9749 (2012).
52. R. F. Lama, B. C. Y. Lu, Excess thermodynamic properties of aqueous alcohol solutions. *J. Chem. Eng. Data* **10**, 216–219 (1965).
53. R. Yan, S. Moon, S. J. Kenny, K. Xu, Spectrally resolved and functional super-resolution microscopy via ultrahigh-throughput single-molecule spectroscopy. *Acc. Chem. Res.* **51**, 697–705 (2018).

54. M. Ovesný, P. Křížek, J. Borkovec, Z. Švindrych, G. M. Hagen, ThunderSTORM: A comprehensive ImageJ plug-in for PALM and STORM data analysis and super-resolution imaging. *Bioinformatics* **30**, 2389–2390 (2014).
55. R. E. Thompson, D. R. Larson, W. W. Webb, Precise nanometer localization analysis for individual fluorescent probes. *Biophys. J.* **82**, 2775–2783 (2002).
56. W. Kohn, L. J. Sham, Self-consistent equations including exchange and correlation effects. *Phys. Rev.* **140**, 5048–5079 (1965).
57. G. Kresse, J. Furthmüller, Efficient iterative schemes for ab initio total-energy calculations using a plane-wave basis set. *Phys. Rev. B Condens. Matter Mater. Phys.* **54**, 11169–11186 (1996).
58. G. Kresse, J. Furthmüller, Efficiency of ab-initio total energy calculations for metals and semiconductors using a plane-wave basis set. *Comput. Mater. Sci.* **6**, 15–50 (1996).
59. J. P. Perdew, K. Burke, M. Ernzerhof, Generalized gradient approximation made simple. *Phys. Rev. Lett.* **77**, 3865–3868 (1996).
60. I. Chorkendorff, J. W. Niemantsverdriet, *Concepts of Modern Catalysis and Kinetics* (Wiley, 2017).
61. M. Levy, Á. Nagy, Variational density-functional theory for an individual excited state. *Phys. Rev. Lett.* **83**, 4361–4364 (1999).
62. S. Plimpton, Fast parallel algorithms for short-range molecular dynamics. *J. Comput. Phys.* **117**, 1–19 (1995).
63. R. C. Dutta, S. Khan, J. K. Singh, Wetting transition of water on graphite and boron-nitride surfaces: A molecular dynamics study. *Fluid Phase Equilib.* **302**, 310–315 (2011).
64. S. J. Stuart, A. B. Tutein, J. A. Harrison, A reactive potential for hydrocarbons with intermolecular interactions. *J. Chem. Phys.* **112**, 6472–6486 (2000).
65. J. Grigera, H. J. C. Berendsen, T. P. Straatsma, The missing term in effective pair potentials. *J. Phys. Chem.* **91**, 6269–6271 (1987).
66. W. L. Jorgensen, D. S. Maxwell, J. Tirado-Rives, Development and testing of the OPLS all-atom force field on conformational energetics and properties of organic liquids. *J. Am. Chem. Soc.* **118**, 11225–11236 (1996).

Acknowledgments: J.C. and A. Radenovic thank M.-L. Bocquet, B. Grosjean, M. Ceriotti, and M. Rossi for discussion. **Funding:** This work was financially supported by a Swiss National Science Foundation (SNSF) support through 200021_192037 grant and National Centre of Competence in Research Bio-Inspired Materials. A. Rayabharam and N.R.A. would like to acknowledge the Center for Enhanced Nanofluidic Transport (CENT), an Energy Frontier Research Center funded by the U.S. Department of Energy, Office of Science, Basic Energy Sciences under award no. DE-SC0019112. A. Rayabharam and N.R.A. also acknowledge the Texas Advanced Computing Center (TACC) at The University of Texas at Austin for providing the computing resources on Stampede2 and Frontera under the allocation TG-CDA100010 and DMR20002, respectively. M.Z. acknowledges the financial support from Swedish Research Council through International Postdoc Grant 2018-06764. **Author contributions:** J.C. conceived the project and designed the experiment. A. Radenovic supervised and coordinated the project. J.C. performed the experiments and data analysis with help from E.G., M.Z., and A.A. A. Rayabharam performed DFT and AIMD simulation under supervision of N.R.A. K.W., and T.T. contributed materials. J.C. wrote the manuscript with input from all authors. **Competing interests:** The authors declare that they have no competing interests. **Data and materials availability:** All data needed to evaluate the conclusions in the paper are present in the paper and/or the Supplementary Materials.

Submitted 1 February 2021

Accepted 6 August 2021

Published 29 September 2021

10.1126/sciadv.abg8568

Citation: J. Comtet, A. Rayabharam, E. Glushkov, M. Zhang, A. Avsar, K. Watanabe, T. Taniguchi, N. R. Aluru, A. Radenovic, Anomalous interfacial dynamics of single proton charges in binary aqueous solutions. *Sci. Adv.* **7**, eabg8568 (2021).

Anomalous interfacial dynamics of single proton charges in binary aqueous solutions

Jean ComtetArchith RayabharamEvgenii GlushkovMiao ZhangAhmet AvsarKenji WatanabeTakashi TaniguchiNarayana R. AluruAleksandra Radenovic

Sci. Adv., 7 (40), eabg8568. • DOI: 10.1126/sciadv.abg8568

View the article online

<https://www.science.org/doi/10.1126/sciadv.abg8568>

Permissions

<https://www.science.org/help/reprints-and-permissions>

Use of think article is subject to the [Terms of service](#)

Science Advances (ISSN) is published by the American Association for the Advancement of Science. 1200 New York Avenue NW, Washington, DC 20005. The title *Science Advances* is a registered trademark of AAAS.
Copyright © 2021 The Authors, some rights reserved; exclusive licensee American Association for the Advancement of Science. No claim to original U.S. Government Works. Distributed under a Creative Commons Attribution NonCommercial License 4.0 (CC BY-NC).